ARTICLE

Check for updates

Direct observation of time-asymmetric breakdown of the standard adiabaticity around an exceptional point

Youngsun Choi[1], Jae Woong Yoon[1✉], Jong Kyun Hong[1], Yeonghwa Ryu[1] & Seok Ho Song [1✉]

Recent study on topological operations around an exceptional point singularity has shown remarkably robust chiral processes that potentially create time-asymmetric or nonreciprocal systems and devices. Nevertheless, direct observation of the entire dynamics in the courses of the topological operations has not been revealed in experiments thus far. Here, we report a comprehensive experimental study on fully time-resolved dynamic-state evolution passages during encircling-an-exceptional-point operations. Using dynamically tunable electrical oscillators, we create a self-intersecting eigenvalue topology with an unprecedented accuracy and experimentally confirm that the time-asymmetric breakdown of the standard adiabaticity is indeed unavoidable when the system encircles an exceptional point in the canonical adiabatic limit. We further discuss the impact of parasitic noises on the time-asymmetric mode-transfer performance and subsequent considerations for practical design requirements.

[1] Department of Physics, Hanyang University, 222 Wangsimni-Ro, Seoul 04763, Korea. ✉email: jaeong.yoon@gmail.com; shsong@hanyang.ac.kr

C ontrolled wave amplification and attenuation are key features for numerous practical devices and systems in acoustics, electronics, and optics. Previously, gain and loss in such systems are in general treated as being independent of major inter-oscillator properties. Remarkable interplay between them has been found only in specific cases such as injection locking and synchronization phenomena[1,2]. However, recent development of the non-Hermitian wave dynamics suggests various novel effects produced by intentionally engaging gain and losses with inter-oscillator or inter-modal coupling properties. They are violation of the Friedel's law of diffraction from stationary lattice structures[3,4], unidirectional invisibility[5,6], broadband optical nonreciprocity[7], to mention a few. Remarkably, exotic non-Hermitian properties have been found even beyond the wave dynamics or classical physics domains as demonstrated in diffusive heat-transfer processes[8] and single-photon systems consisting of a nitrogen vacancy in a diamond crystal[9].

These intriguing effects essentially involve a non-Hermitian singularity referred to as an exceptional point (EP) that corresponds to a threshold of the spontaneous parity-time (PT) symmetry-breaking transition and creates extremely deformed vector spaces due to coalescence of multiple normal-mode solutions[10]. An EP involves a unique self-intersecting Riemann-surface geometry in the parametric eigenvalue spectrum[11,12] that enables an exotic chiral effect under topological stimuli around an EP[7,13–25]. Following the initial theoretical proposal by Moiseyev et al.[13,14], this chiral effect has been experimentally established in microwave transmission channels[17], cryogenic optomechanical oscillators[18], and silicon-photonic waveguide architectures very recently[19]. Therein, final states through the topological operations around an EP strongly suggest that it must involve the chiral mode-transfer effect originating from the time-asymmetric breakdown of the standard adiabaticity. Nevertheless, any direct observation of the effect in the courses of the operations has not been reported thus far. Considering the potential impact of the effect on the fundamental physics and device engineering, direct time-resolved observation of this exotic chiral effect should be an important step toward novel wave-controlling devices and systems pertaining to the far-reaching open-system properties and associated non-Hermitian dynamics.

Here, we provide an experimental analysis that reveals entire dynamics of the time-asymmetric non-Hermitian effect in the courses of the encircling-an-EP (EEP) operations. Using dynamically-tunable electrical-circuit oscillators, we create the Rieman-surface eigenvalue topology with an unprecedented accuracy and measure fully time-resolved complex amplitudes in real-time with the dynamic EEP operations. In contrast to the previous indirect observations due to final-state analyses, the measured dynamic state-evolution passages show how the unique non-Hermitian effects such as the adiabatic state flip, anti-adiabatic state jump, and subsequent time-asymmetric mode transfer properties occur in the passage of time. Therefore, our proposed approach provides a comprehensive experimental platform for fundamental study on exotic non-Hermitian dynamics.

Results

We use dynamically tunable binary electrical-circuit oscillators as shown in Fig. 1. The circuit configuration consists of two capacitively-coupled LRC oscillators. Similar electrical circuits have been used to explore intriguing non-Hermitian properties such as the PT-symmetric quantum brachistochrone problem[26], enhanced remote sensor applications[27,28], anomalous anti-PT-symmetric dynamics[29], and robust wireless power-transfer devices[30]. In our configuration, distinguished features from the

previously studied parity-time-symmetric oscillator circuits[31] are negative-resistor units (partial circuitries with an operational amplifier $A_{\text{L1 or L2}}$, resistors ρ_{NR}, and $A_{\text{R1 or R2}}$) connected in serial with inductor $\lambda_{1 \text{ or } 2}$ and varactor-diode capacitors (d_{C} and d_2) included in the coupling mechanism at C_{C} and the restoration force mechanism at C_2 in Oscillator 2. The negative-resistor units eliminate parasitic resistance components in the inductors. The varactor-diode capacitors provide a control mechanism that dynamically tunes inter-oscillator coupling constant and free-running resonance frequency at Oscillator 2. Other variable components including resistors ρ_{L1}, ρ_{L2}, $\Delta\rho_1$, ρ_{R1}, ρ_{R2}, and a capacitor $\Delta\gamma_1$ are manually tunable so that we precisely adjust an initial condition with a desired set of effective LRC-circuit constants $\{L_1, R_1, C_1, L_2, R_2, C_2\}$. Other details of the circuit configuration are provided in the figure legend for Fig. 1a.

Electrical response of this circuit configuration is described by the following binary Hamiltonian model

$$\frac{d}{dt}|v\rangle = -iH|v\rangle, \quad (1)$$

$$H = \begin{bmatrix} \omega_1 - \kappa + i\gamma & \kappa \\ \kappa & \omega_2 - \kappa \end{bmatrix}, \quad (2)$$

where $|v\rangle = [v_1 \ v_2]^{\text{T}}$ is a state vector with v_n being a voltage-amplitude phasor at Oscillator n, $\omega_n = (L_nC_n)^{-1/2}$ is free-running resonance frequency, $\gamma = (2\Delta\rho_1 C_1)^{-1}$ is decay rate, and $\kappa = \omega_0 C_{\text{C}}(C_1 + C_2)^{-1}$ is a coupling constant with $\omega_0 = 0.5(\omega_1 + \omega_2)$ being average free-running resonance frequency. Here, voltage signal V_n to be measured at Oscillator n is given by $V_n = \text{Re}(v_n)$. The diagonal elements in Eq. (2) consist of free-running resonance frequency ω_n, decay rate γ, and frequency shift κ which is tunable by the varactor-diode capacitors connecting two LC oscillators. See Supplementary Note 1 for detailed mathematical treatment based on the Kirchhoff's circuit laws. In Eq. (2), we note that coupling constant κ in the off-diagonal elements also appears in the diagonal elements in contrast to canonical coupled-oscillator models where diagonal and off-diagonal elements are independent on each other. This property originates from resonance-frequency shift induced by net alternating current passing through the coupling capacitor C_{C}.

The Hamiltonian in Eq. (2) has a parity-time-symmetric EP at $\omega_1 = \omega_2$ and $\gamma = 2\kappa$. Therefore, an EEP operation requires simultaneous control of ω_n and κ around the EP. In our circuit configuration in Fig. 1a, independent electrical tuning of the varactor-diode capacitors at C_{C} and C_2 immediately leads to simultaneous dynamic control of κ and ω_2, respectively.

We realize the required control scenario with a computer-controlled system as illustrated in Fig. 1b. Therein, voltage signals V_{C} and V_{D} from a general purpose AD/DA converter are applied to the varactor-diode capacitors at C_{C} and C_2, respectively, and subsequently adjust κ and ω_2, respectively. A function generator provides an excitation signal to either one of Oscillators 1 or 2 depending on the on/off relay and channel-selecting toggle switch status. An oscilloscope acquires excited signals V_1 and V_2 directly in real time. A desktop computer precisely synchronizes desired control and measurement sequences in communication with the general purpose AD/DA converter, function generator, and the oscilloscope.

In the first step of our experimental analyses, we measure eigenvalues and eigenstates of the system with the circuit constants $L_1 = L_2 = 4.789 \text{ mH}$, $R_1 = 38 \text{ k}\Omega$, R2 = 0, $C_1 = 10 \text{ nF}$, $C_2 = C_1 + \Delta C$ with ΔC varying from -100 pF to $+100 \text{ pF}$, and C_{C} changing from 90 pF to 350 pF. These constants are chosen so that the two oscillators resonate at frequencies around 20 kHz where the equipment that we use here operates in routinely stable and reliable conditions. See "Methods" section and Supplementary Note 2 for
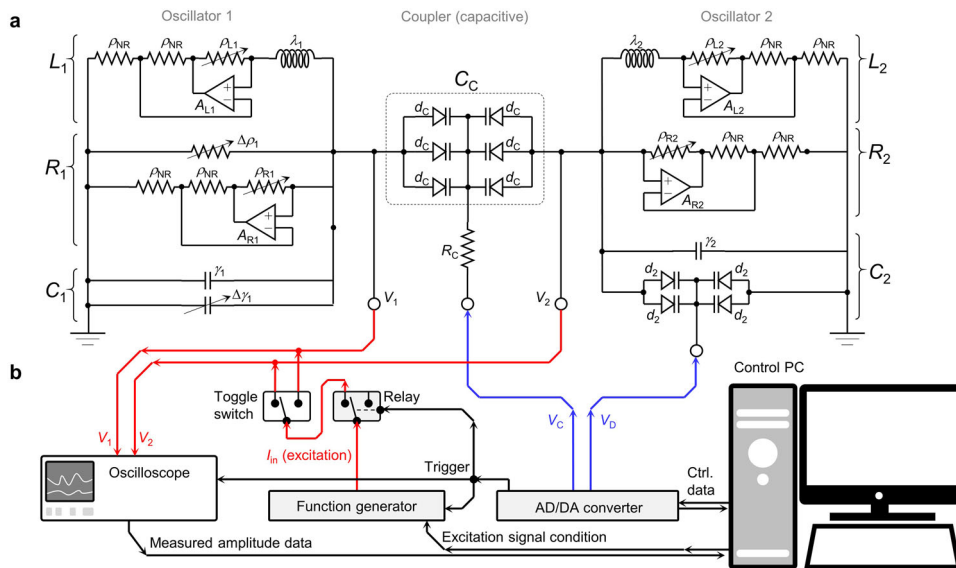
Fig. 1 Binary non-Hermitian Hamiltonian simulator using tunable electrical oscillators. a A circuit diagram for binary electrical oscillators as a dynamic non-Hermitian Hamiltonian simulator. The circuit consists of two LRC oscillators coupled through an electrically-tunable capacitor unit C_C including six varactor diodes (d_C). In Oscillator n, an inductor unit L_n consists of a conventional coil inductor λ_n and a negative-resistance unit (an operational amplifier A_{Ln} and resistors ρ_{NR} and ρ_{Ln}) compensating a parasitic resistance component in λ_n. A resistor unit R_n includes a manually-variable resistor $\Delta\rho_1$ (Oscillator 1 only) and another negative-resistance unit (an operational amplifier A_{Rn} and resistors ρ_{NR} and ρ_{Rn}). A capacitor unit C_n contains a main capacitor γ_n and a manually-variable capacitor $\Delta\gamma_1$ for Oscillator 1 or an electrically-tunable varactor-diode capacitor (four d_2's) for Oscillator 2. **b** Control configuration for dynamically encircling an exceptional point. An excitation signal current I_{in} from a function generator is injected to either one of the two oscillators depending on toggle-switch status. Voltage signals V_C and V_D from an analog-to-digital/digital-to-analog converter dynamically control inter-oscillator coupling constant at C_C and frequency detuning at C_2, respectively. The electrical responses V_1 and V_2 of the two oscillators are acquired with an oscilloscope. The excitation of the circuit and measurement start or stop with a trigger signal from the analog-to-digital/digital-to-analog converter. These controls are precisely managed with a desktop computer (Control desktop computer).

the eigenvalue-measurement procedures and underlying mathematical relations, respectively. Figure 2 shows wireframe surfaces for the measured real and imaginary eigenvalue spectra on a two-dimensional parametric plane represented by ΔC and C_C. Therein, we label a set of eigenvalues for gain modes (or equivalently least-attenuating modes) as λ_G and that for loss modes as λ_L. They clearly show characteristic self-intersecting Riemann-surface geometry around an EP at $(\Delta C, C_C) = (0 \text{ pF}, 185 \text{ pF})$. Remarkably, the experimental and theoretical values agree within an error less than 5 Hz which is merely 0.02% of the minimal resonance frequency identified in this measurement. See Supplementary Fig. 2 for more details. Such high degree of accuracy enables precise further experimental analyses including dynamic EEP operations.

We conduct EEP operations on a parametric loop defined by the relations

$$\Delta C = p A_\Delta \sin(2\pi T^{-1} t), \tag{3}$$

$$C_C = C_0 + A_C \cos(2\pi T^{-1} t)], \tag{4}$$

where p is an encircling-direction parity constant that takes +1 for anticlockwise (ACW) rotation or −1 for clockwise (CW) rotation, A_Δ is an amplitude constant for the ΔC modulation, T denotes a time period for one complete EEP operation, C_0 is an average-capacitance constant for C_C, and A_C are an amplitude constant for the C_C modulation.

Dynamic EEP operations due to this scenario requires a well-prepared initial state $|\psi(0)\rangle$ that should be either one of the two eigenstates, i.e., symmetric-like (bonding) eigenstate $|s\rangle$ or anti-symmetric-like (anti-bonding) eigenstate $|a\rangle$ at our selected starting point $(\Delta C, C_C) = (0 \text{ pF}, 350 \text{ pF})$. This starting point is located in the unbroken PT-symmetric region ($\gamma < 2\kappa$) on the PT-symmetric line at the condition $\omega_1 = \omega_2$. For such initial condition, eigenstates $|s\rangle$ and $|a\rangle$ take identical dissipation rates, i.e.,

identical imaginary eigenvalues. Therefore, there is no preferred state if certain appropriate initial-state preparation procedures are not applied.

We obtain such an initial state by driving the oscillators with time-harmonic current-source signal I_{in} at a measured resonance-center frequency and a subsequent relaxation procedure that effectively eradicates parasitic modal-impurity noises from $|\psi(0)\rangle$. The relaxation procedure is performed by slightly detuning ΔC and C_C towards gain-mode domain for the desired state and then returning to the starting point adiabatically. During this adiabatic process for the initial state preparation, parasitic modal-impurity component exponentially decays in the loss-mode domain while the desired mode component amplifies its amplitude in the gain-mode domain. For an optimally selected adiabatic detuning passage, we achieve desired initial-state with a purity exceeding 99%, as estimated from a real-time excitation-amplitude measurement. Once such a pure initial state is excited from this procedure, control signals V_C and V_D creating ΔC and C_C profiles due to Eqs. (3) and (4) are then injected to perform a single complete round of a desired EEP operation. Meanwhile, excited voltage signals V_1 and V_2 are recorded in time domain as a complete evolution history of an associated dynamic state $|\psi(t)\rangle$. See "Methods" section for further details including associated circuit constants, dynamic control ranges of ΔC and C_C.

The EEP operation in this way successfully produces the theoretically anticipated time-asymmetric mode-transfer effect as shown in Fig. 2 for a time-period constant $T = 30$ ms. Therein, we provide bi-orthogonal expectation value $\langle H \rangle = \langle \psi^*(t)|H|\psi(t)\rangle$ passages with respect to the measured eigenvalue surfaces. The bi-orthogonal expectation value in this way not only allows the simplest probabilistic description for non-Hermitian systems in our case but also can be directly obtained from dynamic-state $|\psi(t)\rangle$ measurement with no need of other
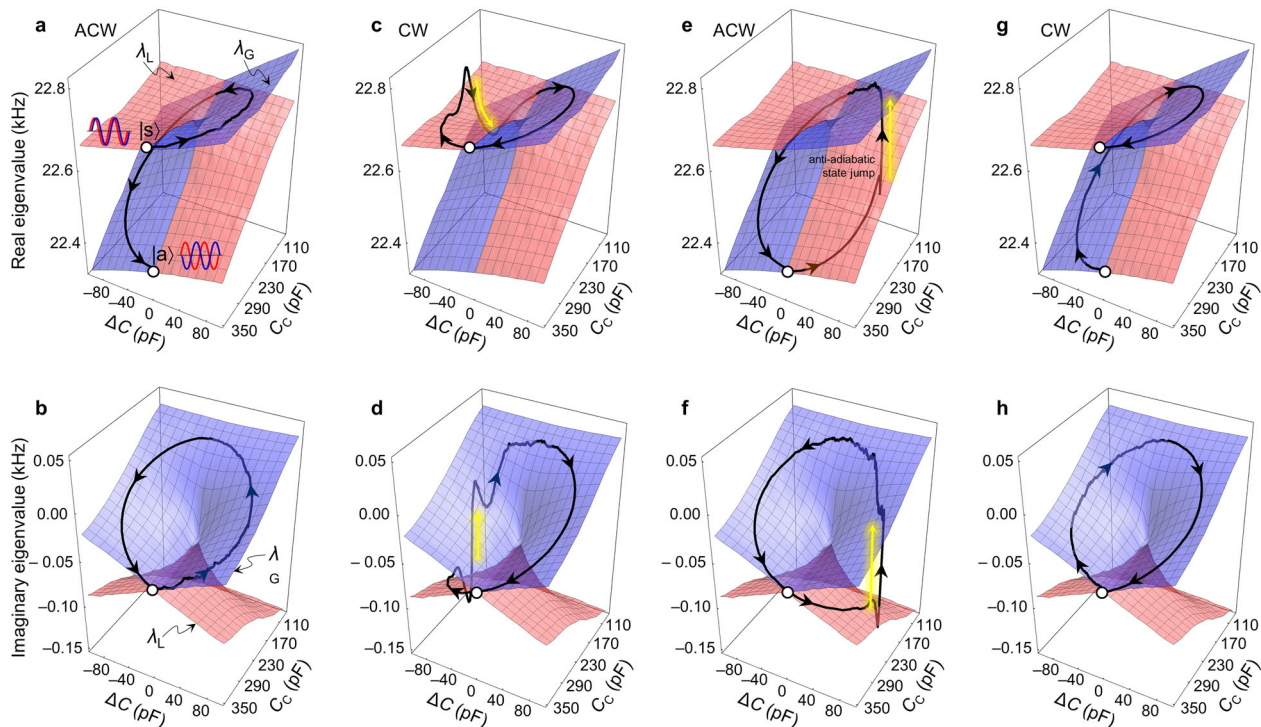
Fig. 2 Complex eigenvalue spectra and dynamic expectation-value passages for encircling-an-exceptional-point operations in experiment. Wireframe surfaces indicate measured real (**a**, **c**, **e**, **g**) and imaginary (**b**, **d**, **f**, **h**) eigenvalues on 2-dimentional (ΔC C_C) plane, where ΔC is detuning capacitance and C_C is coupling capacitance. Eigenvalue surfaces for the gain modes are in light-blue skin and labeled by λ_G while those for the loss modes are in light-red skin and labeled by λ_L. All real and imaginary eigenvalue surfaces in **a**–**h** are duplicated identical plots. Real (**a**, **c**, **e**, **g**) and imaginary (**b**, **d**, **f**, **h**) parts of expectation-value $\langle H \rangle$ passages are indicated by black arrow curves in every panel. Encircling-direction and initial-state conditions for each panel are (**a**, **b**) anticlockwise encircling from $|\psi(0)\rangle = |s\rangle$, (**c**, **d**) clockwise encircling from $|\psi(0)\rangle = |s\rangle$, (**e**, **f**) anticlockwise encircling from $|\psi(0)\rangle = |a\rangle$, and (**g**, **h**) clockwise encircling from $|\psi(0)\rangle = |a\rangle$. Yellow arrows in **c**–**f** indicate portions where anti-adiabatic state-jump events take place. Evolution-time constant T is fixed at 40 ms for all cases in this figure.

independent measurements on eigenvalues and Hamiltonian parameters. See Supplementary Note 3 for detailed explanation. Note that Fig. 2a, b show ACW ($p = +1$) EEP case and Fig. 2c, d show CW ($p = -1$) case for an initial state $|\psi(0)\rangle = |s\rangle$. The real and imaginary parts of $\langle H \rangle$ passages in the ACW case adiabatically evolve from the initial eigenvalue point for $|s\rangle$ to that for $|a\rangle$ while $\langle H \rangle$ passages in the CW case involve the anti-adiabatic state jump from the loss-mode (λ_L) surface to the gain-mode (λ_G) surface and the passages eventually end up in the eigenvalue point for $|s\rangle$).

Here, the essential physics is a fact that an EEP operation on a loss-mode surface inevitably undergoes an anti-adiabatic state jump toward a gain-mode surface while the time-reversed operation simply evolves along the adiabatic-state passage on a gain-mode surface. This property is clearly found in the other cases for $|\psi(0)\rangle = |a\rangle$ as shown in Fig. 2e–h.

Discussion
Our electrical-circuit EEP simulator enables further experimental investigation on various parametric dependences of the time-asymmetric EEP operations. For a given EEP loop, a parameter of the most significant impact is the evolution-time constant T because it is a characteristic time scale of the EEP operation that is directly associated with the time-asymmetric mode-transfer efficiency[18]. In Fig. 3, we provide measured $\langle H \rangle$ passages for different T values in a range from 2 ms to 50 ms. It shows measured passages for all four possible cases from the two encircling-direction and two initial-state conditions. The adiabatic state flip takes place for the CCW case with initial state $|s\rangle$ (Fig. 3a) and CW case with initial state $|a\rangle$ (Fig. 3b). They experimentally demonstrate the time-asymmetric mode-transfer effect persisting

over a broad T ranges. Importantly, Fig. 3c, d show significant details of the anti-adiabatic jump that has never been observed in experiments previously.

In the time-resolved passages during the anti-adiabatic state jump, we note two important observations. First, this state jump obviously becomes inevitable for larger T values as the binary Hamiltonian model predicts[18]. Therefore, we experimentally confirm that this effect is indeed *anti-adiabatic* in a sense that slower parametric change makes the abrupt non-adiabatic transition unavoidable.

Another important observation is that the passages during the jump seem remarkably chaotic for excessively large T values ($T >$ 40 ms in our measurement). In our analyses, this property does not appear for ideal cases in theoretical study and becomes prominent whenever amplitude of the dynamic state $|\psi(t)\rangle$ is comparable to noise levels. Therefore, the chaotic behavior of the passages during the jump is attributed to amplified noises in the gain mode that dominate system's response when the dynamic state before the jump stays at the loss mode for a significantly long time enough to attenuate its amplitude below a certain critical level. Developing practical device applications, this implies that care must be taken for device design in this aspect. The evolution-time constant T should be in a certain optimal range in order to avoid chaotic signal behaviors and to maintain certain encoded information carried by the dynamic states through the time-asymmetric EEP operations.

Further investigating the optimal range of the T values for a given EEP loop, we take a closer look at modal probability $P_G(t)$ $= |\langle \phi_G^* | \psi(t) \rangle|^2$ and $P_L(t) = |\langle \phi_L^* | \psi(t) \rangle|^2$ curves in time domain, where $|\phi_G\rangle$ and $|\phi_L\rangle$ represent the gain and loss modes
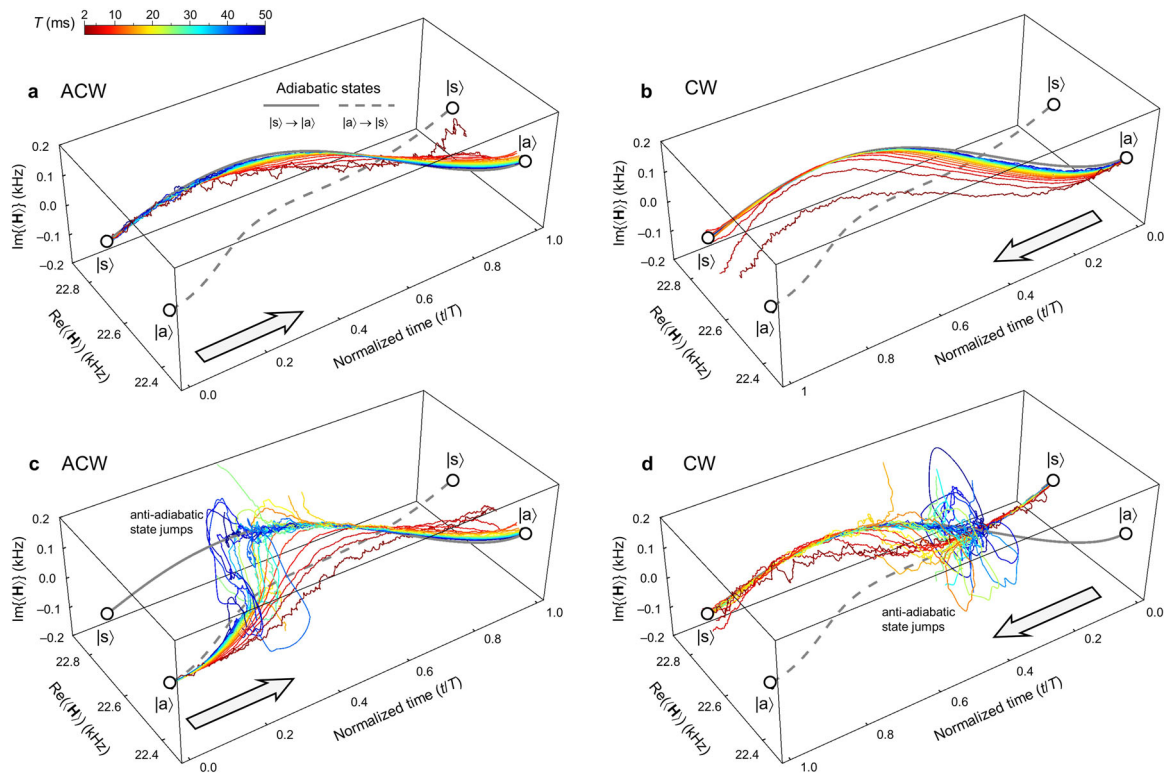
Fig. 3 Evolution passages of dynamic states in time domain. Complex expectation value $\langle H \rangle$ as a function of passage time t for different evolution-time constant T. Encircling-direction and initial-state conditions for each panel are (**a**) anticlockwise encircling from $|\psi(0)\rangle = |s\rangle$, (**b**) clockwise encircling from $|\psi(0)\rangle = |a\rangle$, (**c**) anticlockwise encircling from $|\psi(0)\rangle = |a\rangle$, and (**d**) clockwise encircling from $|\psi(0)\rangle = |s\rangle$. Colors of the expectation-value $\langle H \rangle$ passage curves indicate corresponding evolution-time constant T values in a 2-to-50-ms range as represented by the horizontal color-density bar above panel **a**. Gray curves in each panel indicate reference passages if a state follows the exact instantaneous eigenstates, i.e., adiabatic states, along the EEP loop. Light-gray arrow on the bottom of panel indicates the evolution-time direction.

corresponding to the eigenvalues $\lambda_{\rm G}$ and $\lambda_{\rm L}$, respectively. These curves are inferred from the measured complex amplitudes and are shown in Fig. 4. In Fig. 4a for the ACW EEP cases with initial-state condition $|\psi(0)\rangle = |s\rangle$, the EEP operations do not involve the anti-adiabatic state jump and it results in $P_{\rm G}(t) \approx 1$ and $P_{\rm L}(t) \approx 0$ over the entire time domain from 0 to T. Significant deviation of $P_{\rm G}(t)$ from 1 and $P_{\rm L}(t)$ from 0 is found only for $T < 5$ ms. In this case, non-adiabatic coupling is strong due to fast parametric change beyond the standard adiabatic limit. Almost identical property is also found for CW EEP cases starting from $|\psi(0)\rangle = |s\rangle$, as shown in Fig. 4b. Therefore, in order to induce efficient EEP operations for the adiabatic state flip, a necessary condition is to have a sufficiently large T so that $|\psi(t)\rangle$ undergoes time-varying system configuration well within the canonical adiabatic limit.

For stable EEP operations involving the anti-adiabatic state jump, on the other hand, T does not have to be excessively large. Modal-probability curves involving the anti-adiabatic state jump are provided in Fig. 4c, d. In these cases, the curves start at $P_{\rm G}(0) = 0$ and $P_{\rm L}(0) = 1$, undergo abrupt transitions associated with the anti-adiabatic state jump near $t \approx 0.4\,T$, and finally relax at $P_{\rm G} \approx 1$ and $P_{\rm L}(t) \approx 0$ as the dynamic states settle down in the gain-mode ($|\phi_{\rm G}\rangle$) passage in each case. We notice that the curves toward $t = T$ indicate that the dynamic states end up in a single-mode state $|\psi(T)\rangle \approx |\phi_{\rm G}\rangle$ for $T > 20$ ms and, thereby, excessively large T over 20 ms should not offer any remarkable advantage for the time-asymmetric EEP operations.

Moreover, dynamic responses of the system during the anti-adiabatic state jump become significantly instable due to noise-

induced chaotic behaviors for excessively large T as signal strength of $|\psi(t)\rangle$ tends to enter the low signal regime where unpredictable noises present in general. Therefore, optimal dynamic-control speed conditions for given noise levels should be taken into account as a crucial design requirement for practical device applications.

In summary, we have developed a dynamic non-Hermitian simulator using tunable electrical-circuit oscillators. The proposed electrical-circuit simulator creates characteristic non-Hermitian spectral structures with unprecedented accuracy and enables fully time-resolved complex-amplitude measurements for unique non-Hermitian effects such as the adiabatic state flip, anti-adiabatic state jump, and time-asymmetric mode-transfer operation. Notably, arbitrary EEP loops and evolution-speed profiles are immediately realizable simply by injecting appropriately prepared control signals $V_{\rm C}$ and $V_{\rm D}$ in our proposed approach. As a reliable experimental test platform for emerging non-Hermitian physics and concomitant device applications, the tunable electrical-oscillator approach takes remarkable advantages in terms of simplicity in construction, flexibility in configuring desired non-Hermitian Hamiltonians, high control precision, and fully time-resolved measurement capability without any significant interruption of the excited state. Therefore, our proposed method is immediately applicable as a real-time simulator for dynamic non-Hermitian properties. Further development involving higher-order EPs or nonlinear components is greatly of interest for advanced experimental investigation on various non-Hermitian effects and their potential applications.
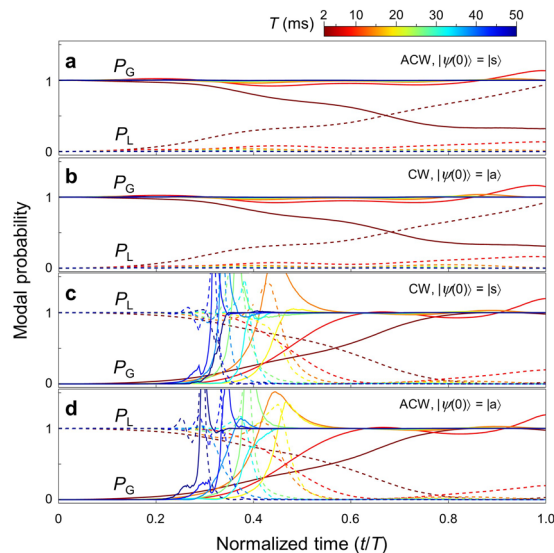
Fig. 4 Dependence of modal probability passage on evolution-time constant T. Modal probability P_G (gain mode) and P_L (loss mode) curves (solid and dashed curves, respectively) at different evolution-time constant T as a function of passage time t. Encircling-direction and initial-state conditions for each panel are (**a**) anticlockwise encircling from $|\psi(0)\rangle = |s\rangle$, (**b**) clockwise encircling from $|\psi(0)\rangle = |a\rangle$, (**c**) clockwise encircling from $|\psi(0)\rangle = |s\rangle$, and (**d**) anticlockwise encircling from $|\psi(0)\rangle = a\rangle$. Color scheme for curves for different T is identical to that in Fig. 3. The probability curves are inferred by bi-orthogonal inner product $P_G = |\langle\phi_G^*|\psi\rangle|^2$ and $P_L = |\langle\phi_L^*|\psi\rangle|^2$ with experimentally obtained dynamic state $|\psi\rangle$. $|\phi_G\rangle$ and $|\phi_L\rangle$ denote the gain and loss modes, respectively.

Methods

Eigenvalue-measurement procedures. In our eigenvalue-measurement method, we excite the circuit for given ΔC and C_C with a time-harmonic current I_{in} at a frequency f_n and an amplitude of 0.5 μA injected at Oscillator 1, wait for 100 ms until response of the circuit relaxes at a stationary state, take $V_2(t)$ at Oscillator 2 in time domain over 10 ms, identify oscillating amplitude $a_2(f_n)$ from $V_2(t)$, and repeat this measurement cycle for $a_2(f_{n+1})$ at a next excitation frequency f_{n+1}. Real and imaginary parts, i.e., $\text{Re}(\lambda)$ and $\text{Im}(\lambda)$, respectively, of the eigenvalue of H are identified by double-Lorentzian curve fitting of an acquired amplitude spectrum $\{a_2(f_n)\}$ for resonance-peak center frequencies and linewidths, respectively.

Circuit constants for the EEP operation. In our dynamic EEP-operation experiment, fixed constants are $A_\Delta = 80$ pF, $A_C = 120$ pF, and $C_0 = 230$ pF, while p and T are taken as case-by-case variables in order to investigate corresponding changes in the dynamic state passages. Under this condition, corresponding EEP loop is an ellipse starting at $(\Delta C, C_C) = (0$ pF, 350 pF$)$ and inscribing a rectangular area within -80 pF $\leq \Delta C \leq +80$ pF and 110 pF $\leq C_C \leq 350$ pF ranges. In addition, we detune R_2 off zero in a negative region of -200 kΩ $< R_2 < 0$ ($R_2 \sim -115$ kΩ in the EEP measurements) so that excited signals in the oscillators stay acceptably high with respect to a noise level ~ 2 mV in our laboratory environment and do not go beyond upper and lower amplifier thresholds at $+10$ V and -10 V, respectively. We note that R_2 detuning in this way does not affect the established eigen-system structure since it changes the corresponding Hamiltonian in a specific way following $H \rightarrow H' = H - igI$, where g is an auxiliary gain coefficient and I is the identity operator. The amount of eigenvalue splitting and subsequent dynamic properties of the relative system responses are invariant for any change under this constraint. The only consequence of the R_2 detuning is overall amplitude change in the excited signals while essential dynamics in relative signal amplitudes remain unspoiled in principle as far as the amplification and attenuation processes in the system operates in the linear regime.

Data availability

The data that support the findings of this study are available from the corresponding author upon reasonable request.

References

1. Adler, R. A study of locking phenomena in oscillators. *Proc. IRE* **34**, 351–357 (1946).
2. Paciorek, L. J. Injection locking of oscillators. *Proc. IEEE* **53**, 1723–1727 (1965).
3. Hahn, C. et al. Observation of exceptional points in reconfigurable non-Hermitian vector-field holographic lattices. *Nat. Commun.* **7**, 12201 (2016).
4. Jia, Y., Yan, Y., Kesava, S. V., Gomez, E. D. & Giebink, N. C. Passive parity-time symmetry in organic thin film waveguides. *ACS Photon.* **2**, 319–325 (2015).
5. Feng, L. et al. Experimental demonstration of a unidirectional reflectionless parity-time metamaterial at optical frequencies. *Nat. Mater.* **12**, 108–113 (2013).
6. Lin, Z. et al. Unidirectional invisibility induced by PT-symmetric periodic structures. *Phys. Rev. Lett.* **106**, 213901 (2011).
7. Choi, Y., Hahn, C., Yoon, J. W., Song, S. H. & Berini, P. Extremely broadband, on-chip optical nonreciprocity enabled by mimicking nonlinear anti-adiabatic quantum jumps near exceptional points. *Nat. Commun.* **8**, 14154 (2017).
8. Li, Y. et al. Anti-parity-time symmetry in diffusive systems. *Science* **364**, 170–173 (2019).
9. Wu, Y. et al. Observation of parity-time symmetry breaking in a single-spin system. *Science* **364**, 878–880 (2019).
10. El-Ganainy, R. et al. Non-Hermitian physics and PT symmetry. *Nat. Phys.* **14**, 11–19 (2018).
11. Dembowski, C. et al. Experimental observation of the topological structure of exceptional points. *Phys. Rev. Lett.* **86**, 787–790 (2001).
12. Gao, T. et al. Observation of non-Hermitian degeneracies in a chaotic exciton-polariton billiard. *Nature* **526**, 554–558 (2015).
13. Uzdin, R., Mailybaev, A. & Moiseyev, N. On the observability and asymmetry of adiabatic state flips generated by exceptional points. *J. Phys. A* **44**, 435302 (2011).
14. Gilary, I., Mailybaev, A. A. & Moiseyev, N. Time-asymmetric quantum-state-exchange mechanism. *Phys. Rev. A* **88**, 010102(R) (2013).
15. Milburn, T. J. et al. General description of quasiadiabatic dynamical phenomena near exceptional points. *Phys. Rev. A* **92**, 052124 (2015).
16. Hassan, A. U., Zhen, B., Soljačić, M., Khajavikhan, M. & Christodoulides, D. N. Dynamically encircling exceptional points: exact evolution and polarization state conversion. *Phys. Rev. Lett.* **118**, 093002 (2017).
17. Doppler, J. et al. Dynamically encircling an exceptional point for asymmetric mode switching. *Nature* **537**, 76–79 (2016).
18. Xu, H., Mason, D., Jiang, L. & Harris, J. G. E. Topological energy transfer in an optomechanical system with exceptional points. *Nature* **537**, 80–83 (2016).
19. Yoon, J. W. et al. Time-asymmetric loop around an exceptional point over the full optical communications band. *Nature* **562**, 86–90 (2018).
20. Ghosh, S. N. & Chong, Y. D. Exceptional points and asymmetric mode conversion in quasi-guided dual-mode optical waveguides. *Sci. Rep.* **6**, 19837 (2016).
21. Zhang, X. L., Wang, S., Hou, B. & Chan, C. T. Dynamically encircling exceptional points: in situ control of encircling loops and the role of the starting point. *Phys. Rev. X* **8**, 21066 (2018).
22. Zhang, X. L., Jiang, T. & Chan, C. T. Dynamically encircling an exceptional point in anti-parity-time symmetric systems: asymmetric mode switching for symmetry-broken modes. *Light Sci. Appl.* **8**, 88 (2019).
23. Graefe, E.-M., Mailybaev, A. A. & Moiseyev, N. Breakdown of adiabatic transfer of light in waveguides in the presence of absorption. *Phys. Rev. A* **88**, 033842 (2013).
24. Kaprálová-Žďánská, P. R. & Moiseyev, N. Helium in chirped laser fields as a time-asymmetric atomic switch. *J. Chem. Phys.* **141**, 014307 (2014).
25. Fernández-Alcázar, L. J., Li, H., Ellis, F., Alú, A. & Kottos, T. Robust scattered fields from adiabatically driven targets around exceptional points. *Phys. Rev. Lett.* **124**, 133905 (2020).
26. Ramezani, H., Schindler, J., Ellis, F. M., Günther, U. & Kottos, T. Bypassing the bandwidth theorem with PT symmetry. *Phys. Rev. A* **85**, 062122 (2012).
27. Chen, P. et al. Generalized parity–time symmetry condition for enhanced sensor telemetry. *Nat. Electron.* **1**, 297–304 (2018).
28. Sakhdari, M. et al. Experimental observation of PT symmetry breaking near divergent exceptional points. *Phys. Rev. Lett.* **123**, 193901 (2019).
29. Choi, Y., Hahn, C., Yoon, J. W. & Song, S. H. Observation of an anti-PT-symmetric exceptional point and energy-difference conserving dynamics in electrical circuit resonators. *Nat. Commun.* **9**, 1–6 (2018).
30. Assawaworrarit, S., Yu, X. & Fan, S. Robust wireless power transfer using a nonlinear parity–time-symmetric circuit. *Nature* **546**, 387–390 (2017).
31. Schindler, J., Li, A., Zheng, M. C., Ellis, F. M. & Kottos, T. Experimental study of active LRC circuits with PT symmetries. *Phys. Rev. A* **84**, 040101(R) (2011).

Author contributions

Y.C., J.W.Y., and S.H.S. conceived the original concept and initiated the work. Y.C and J.W.Y. developed the theory and model. Y.C., J.K.H., and Y.R. designed the circuit board. Y.C. and J.W.Y. performed EEP measurements. Y.C., J.W.Y., and S.H.S. analyzed the measurement results. All authors discussed the results. J.W.Y., Y.C., and S.H.S. wrote the manuscript.

Competing interests

The authors declare no competing interests.

Additional information

Supplementary information is available for this paper at https://doi.org/10.1038/s42005-020-00409-y.

Correspondence and requests for materials should be addressed to J.W.Y. or S.H.S.